ARCHIVES
OF THERMODYNAMICS

Numerical investigation of thermal-flow processes in the ejector-condenser for selected geometrical parameters

Tomasz Kuś[*], Paweł Madejski

AGH University of Krakow, Faculty of Mechanical Engineering and Robotics, Department of Power Systems and Environmental
Protection Facilities, al. Mickiewicza 30, 30-059 Kraków, Poland
*Corresponding author email: kus@agh.edu.pl

Abstract

The paper presents the results of analysis of thermal-flow processes in the ejector-condenser for selected geometrical parameters using CFD (Computational Fluid Dynamics) methods. The ejector-condenser is the water-driven, two-phase ejector responsible for creating a sub-pressure allowing exhaust gases (steam and CO_2 mixture) to be entrained, condensing steam, and then increasing the pressure above the atmospheric conditions. The axisymmetric numerical model was developed to take into account multiphase, turbulent flow with steam condensation in the presence of inert gas. The influence of the selected geometrical parameters, such as the motive nozzle's and mixing chamber's diameters on the ejector performance was investigated. CFD analysis results are presented in the form of developed scalar distributions as well as pressure, temperature and steam mass flow changes along the flow path. Performances for different geometry modes were calculated and compared using parameters such as compression ratio, expansion ratio, mass entertainment ratio and condensation efficiency. The maximum achieved compression ratio for the analyzed geometrical variants is 1.113 for the assumed mass entertainment ratio of 0.0295. The condensation efficiency varies in a range of 49.6%–91.4% depending on motive fluid inlet conditions and geometry mode.

Keywords: Ejector; Two-phase flow, Steam condensation, Computational fluid dynamics

1. Introduction

Ejectors are highly reliable, almost free-maintenance and have no moving parts. They can be used for transporting and compressing fluids and carrying out heat and mass transfer processes. For an efficient operation, the proper design is needed to minimize flow losses. Numerical modelling gives a possibility to investigate and understand more deeply the influence of various design and operating parameters on the ejector performance.

Because of complex phenomena, which take place especially in the ejectors, researchers more and more often are using CFD (Computational Fluid Dynamics) modelling to take into account turbulent flow with heat and mass transfer processes, when the ejector is working in two-phase mode.

Modelling of the flow in one-phase ejectors is connected with the appropriate reflection of the turbulent flow and thermophysical properties of fluids, which is especially important when dealing with gas ejectors working in subsonic and supersonic modes [1]. In one-phase ejectors, the momentum exchange occurs as a result of turbulence, shock train formation and boundary layer interactions [2].

A 3D CFD model of the one-phase water ejector to compute friction losses was developed by Marum et al. [3]. Three different turbulence models were used to calculate incompressible flow in the ejector and the $k-\omega$ SST model turned out to be the most suitable. Various turbulent approaches (standard $k-\varepsilon$,

Nomenclature

a – interfacial area per unit volume / interaction area density, 1/m
$\boldsymbol{a}$ – surface area vector, m^2
A – surface area, m^2
C – coefficient,
f – dumping functions
$\boldsymbol{f}_b$ – body force vector, N/m^3
$\dot{g}$ – mass flow rate boiling/condensation per unit volume, $kg/(m^3 s)$
h – heat transfer coefficient, $W/(m^2 K)$
H – total enthalpy, m^2/s^2
$\mathbf{I}$ – unit tensor
k – turbulent kinetic energy, J/kg
l – interaction length scale, m
L – phase change heat, J/kg
$\dot{m}$ – mass flow rate of steam, kg/s
N – pressure ratio
Nu – Nusselt number
p – pressure, Pa
P – production term, W/m^3
Pr – Prandtl number
r – radius, m
Re – Reynolds number
$\dot{q}$ – heat flux vector, W/m^2
Q – heat transfer per unit volume, W/m^3
S – source term, W/m^3 or 1/s
Sc – Schmidt number
t – time scale, s
T – temperature, K
$\mathbf{T}$ – viscous stress tensor, Pa
$\boldsymbol{v}$ – velocity, m/s
V – volume, m^3

Greek symbols

α – volume fraction
γ – temperature ratio
ε – turbulent dissipation rate, J/(kg s)
η – condensation efficiency, %
θ – expansion ratio
λ – heat conductivity, W/(m K)
μ – dynamic viscosity, Pa·s
ξ – compression ratio
ρ – density, kg/m^3
σ – coefficient
τ – stresses, Pa

Subscripts

0 – specific/ambient value
$1,2$ – ordering numbers
c – continuous phase
CO_2 – carbon dioxide
d – at driving fluid inlet
e – energy/large eddy
g – at gas inlet
i – phase i
j – phase j
k – turbulent kinetic energy
m – mixture
o – at diffuser outlet
s – steam
t – turbulent
u – phase
w – water
ε – turbulent dissipation rate
Θ – angular direction
μ – viscosity

Abbreviations and Acronyms

CFD – computational fluid dynamics
FVM – finite volume method
XNP – nozzle exit position

RNG $k–\varepsilon$, realizable $k–\varepsilon$ and $k–\omega$ SST) using CFD techniques for modelling of the supersonic steam ejector were tested by Xiao et al.[4]. The level of agreement with experimental data of each model depends on various factors: the solver type (pressure vs. density based, mesh density, discretization scheme. The $k–\omega$ SST and realizable $k–\varepsilon$ models with the two wall treatments are recommended.

Two-phase ejector modelling is much more challenging due to complicated gas-liquid interfacial interactions and the possibility of mass transfer between the phases. Therefore, knowledge of thermodynamic and mechanical non-equilibrium effects is crucial to develop reliable numerical models [5].

Koirala et al. [6] numerically investigated two-phase flow with condensation in a water-driven steam ejector using the Eulerian method with a thermal phase-change model. Results show that the numerical model is an effective tool for solving complex flow with a phase change. A two-phase ejector operating with LNG (liquefied natural gas) as motive fluid and BOG (boiling off gas) as entrained fluid with the condensation process was computed using the CFD technique by Zheng et al. [7]. A mixture model with the standard $k–\varepsilon$ model was applied. Assari et al. [8] conducted numerical research where the water-air ejector was modelled using two different approaches: Eulerian-Eulerian and mixture. The mixture model seems to be more efficient considering computational time, convergence and consistency with experimental data.

Computational research leading to a better understanding of the jet behaviour and gas induction in a liquid-gas ejector was conducted by Sharma et al. [9]. The axisymmetric model with the Euler-Euler framework combined with the standard $k–\varepsilon$ model was developed. It was concluded that adding the turbulent dispersion model causes the phase profile more dispersed. The mixing process of liquid and gas in the ejector was investigated by Wang et. al. [10] using the numerical model based on the steady-state two-fluid mixture model and realizable $k–\varepsilon$ model. The turbulent mixing process was indicated as the most efficient mechanism. The influence of applying various turbulence models on the two-phase CO_2 ejector operation was investigated by Majchrzyk et al. [11]. Multiphase flow was calculated using a homogeneous equilibrium model (HEM) taking into account real properties. The Reynolds Stress Model with linear pressure-strain approach gives the best prediction.

Operating conditions, working medium and design factors influence the ejector performance. In this study, attention will be focused on those listed last. The performance is investigated mainly using dimensionless quantity like compression ratio, pressure ratio or entrainment ratio (volumetric or mass flow), Madejski et al. [12]. In the paper [12], the authors confirmed by simulation results with adopted characteristic curves of ejector operation that the mass flow rate of water strongly depends on the ejector design and entrainment ratio.

CFD investigation of the nozzle diameter, nozzle exit position (NXP), mixing length, diffuser curve and diameter in water-water ejector was investigated by Reis et al. [13]. The following performance indicators were obtained: pressure ratio: 0.2–0.8; efficiency: 0–35%; entrainment ratio (volumetric): 0–7. In the optimized geometry, flow profiles are more homogeneous which is more profitable − less dissipative. The influence of the diffuser angle, mixing chamber length and nozzle position on the water-water ejector performance was investigated using CFD by Sheha et al. [14]. The obtained pressure ratio was in the range of 0.37–0.8 and the entrainment mass ratio up to 2. The maximum obtained efficiency was 37.8% for the optimal design. The entrainment ratio in the range of 0.5–2.6 for different chamber heights, mixing and diffuser diameters for the assumed compression ratios 1 and 1.17 was computed for an air-air ejector by Zhang et al. [15] using numerical simulation. Too small geometrical parameters lead to an increase in total pressure losses influenced by the shock wave intensity. The influence of NXP on the operation of an air-air (air+water) ejector was investigated numerically and experimentally by Chen et al. [16]. The obtained pressure ratio: 0.04–0.29 and entrainment ratio: 0.05–0.45. The optimum NXP depends on the water mass flow rate and operation mode (one-phase, two-phase, critical, subcritical). The liquid content in the gas phase for different mixing chamber lengths was investigated by Yan et al. [17] using CFD.

The achieved entrainment ratio was 0.15–0.45 and the optimal length varied depending on the liquid content in gases. Mohammadi [18] investigated numerically (CFD) the influence of the nozzle diameter, mixing chamber diameter, throat diameter, nozzle exit position on the multistage steam-air ejector performance. The following nondimensional parameters were obtained: compression ratio: 2.875, 4.25, 12.219 (multi-stage), the multistage ejector gives the possibility to achieve a high compression ratio compared to the single stage ejector.

Considering steam-steam ejectors, Foroozesh et al. [19] calculated, using the CFD method, the ejector operation for various throat diameters of the primary nozzle. The achieved entrainment ratio was in the range of 0.31–0.51. As a result of optimization, the entrainment ratio was improved by about 32%.

Dong et al. [20], conducted CFD analysis of the influence of the mixing chamber length on the entrainment ratio and critical back pressure in a steam ejector. The entrainment ratio was up to 0.7 and the critical back pressure: 1.3–3.7 kPa. A too long mixing chamber leads to a decrease in entrainment ratio and critical back pressure. Han et al. [21] investigated the steam ejector performance for different throat diameters and NXPs using CFD. The achieved volumetric entrainment ratio was 0.01–1.2 and pressure ratio 0.0827. An excessively small or large throat diameter and too large NXP strengthen the boundary layer separation.

In the analyzed solution of the ejector-condenser, the stream of primary fluid leaves the nozzle cross-section in a discrete form with a huge number of droplets. In the beginning, the water jet form can be noticed and the break-up of the jet depends on the physical properties of the fluids, surface tension and velocity [22]. The velocity of the outflow stream depends on the nozzle shape. A number of small-scale phenomena occur inside the nozzle [23–26], which affect the global characteristics of the device. Even when applying the most advanced 2D/3D numerical models, experimental investigation for verification of the results is required. The complex phenomenon inside two-phase ejector-condensers requires an advanced test stand to monitor thermal and flow conditions changing through the flow inside the ejector condenser. Madejski et al. [27,28] proposed assumptions and guidelines for building a prototype experimental test-rig installation for experimental research on direct contact condensers. Pressure change and temperature change along the flow of the mixture have to be monitored simultaneously because of the high instability of this phenomenon, which is also visible during CFD studies.

This paper presents results of numerical investigations of the ejector condenser, designed to entrain steam-CO_2 mixture and condense steam with the presence of inert gas. A basic geometrical model has been developed to provide the most efficient condensation process. The expected compression ratio resulting from the created sub-pressure at the gas inlet is relatively low (max. 1.25). A CFD model with the use of mixture approach and realizable two-layer $k-\varepsilon$ turbulence model was used to develop a numerical model of the ejector condenser, allowing us to capture the phenomenon complexity. The influence of changing geometrical parameters on the ejector performance was evaluated.

2. The object of the research

The research object is the ejector condenser, which is part of the Negative CO_2 Emission Gas Power Plant [29]. The scheme of the ejector is presented in Fig. 1, and detailed dimensions for the basic model are presented in Table 1.
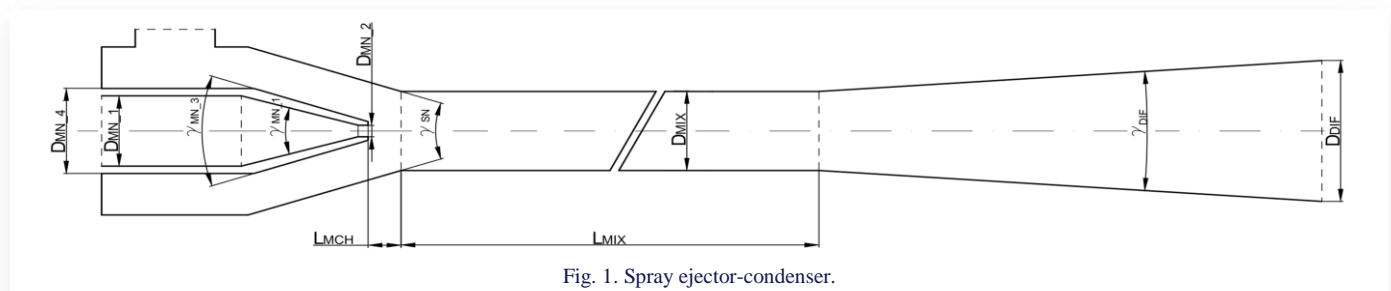

Fig. 1. Spray ejector-condenser.

Table 1. Ejector-condenser dimensions.

Parameter	Value	Parameter	Value	Parameter	Value
D_{MN_1}[mm]	25.4	D_{DIF} [mm]	100.0	γ_{MN_3} [°]	45.0
D_{MN_2}[mm]	3.0	L_{MIX} [mm]	1050.0	γ_{SN} [°]	45.0
D_{MN_4}[mm]	40.0	L_{MCH} [mm]	25.0	γ_{DIF} [°]	10.0
D_{MIX} [mm]	25.4	γ_{MN_1} [°]	30.0	-	-

3. Numerical model

3.1. Assumptions and boundary conditions

The axisymmetric numerical model was developed using a Simcenter STAR-CCM+ software based on the finite volume method (FVM). Model parameters at the boundary surfaces are presented in Fig. 2. Water properties are assumed to be constant. Steam and CO_2 properties are assumed to be temperature-dependent based on the IAPWS-IF97 [30] and NIST library [31], respectively.
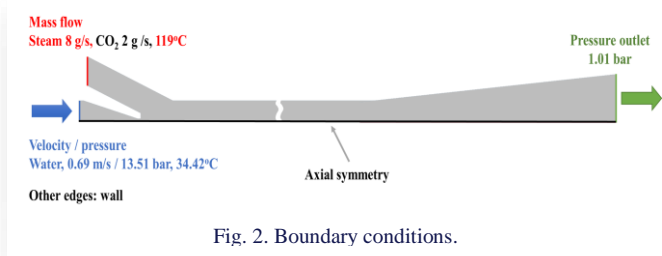

Fig. 2. Boundary conditions.

3.2. Numerical mesh

The polyhedral-elements-based mesh was developed. Mesh-sensitivity analysis was conducted based on the pressure charts along the flow path for meshes with different base sizes presented in Fig. 3. The pressure measurement points were located directly near the wall and the presented length is a distance from the motive nozzle outlet. Meshes 1–5 are characterized by the following number of elements: 60 787, 174 895, 387 221, 820 753, and 1 302 936. Taking into account the change of the solution during mesh refinement, the stability of the calculation and the available computing power, mesh 4 was selected.
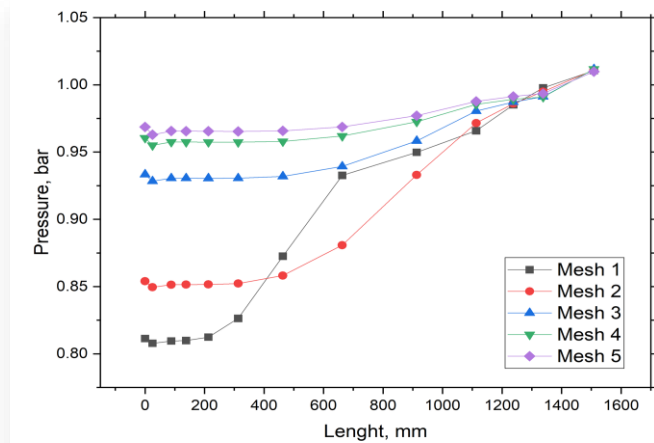

Fig. 3. Mesh independence study for ejector-condenser numerical analysis (0 mm – motive nozzle outlet).

The suction chamber and the beginning of the mixing chamber for mesh 4 is presented in Fig. 4.
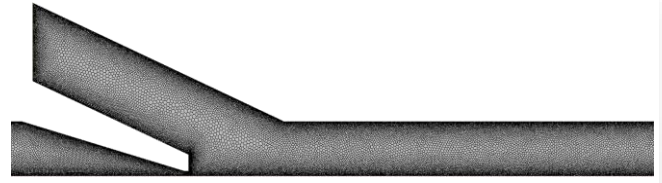

Fig. 4. Mesh at the suction chamber and at the beginning of the mixing chamber.

The base size of the chosen mesh element is 0.077 mm. It gives 820 753 elements for basic geometry and differs slightly depending on the geometry modification. The inflation layer is applied with the following properties: 3 layers, 0.03 mm total thickness and 1.6 growth ratio. The mesh was also locally refined, e.g. at the motive nozzle's trailing edge, where large pressure and velocity gradients occur.

3.3. Parameters definition

The main parameters in this paper include the compression ratio, expansion ratio, pressure ratio, mass entrainment ratio, temperature ratio and condensation efficiency.

The compression ratio ξ is the ratio between the pressures at the diffuser outlet p_o and gas inlet p_g (Eq. (1)):

$$\xi = \frac{p_o}{p_g}. \tag{1}$$

The expansion ratio θ is the ratio between the pressures at the driving fluid inlet p_d and gas inlet p_g (Eq. (2)):

$$\theta = \frac{p_d}{p_g}. \tag{2}$$

The pressure ratio N is expressed in terms of pressures at the inlets: p_g, p_d and diffuser outlet p_o (Eq. (3)):

$$N = \frac{p_o - p_g}{p_d - p_o}. \tag{3}$$

The temperature ratio k is expressed in terms of temperatures at the inlets: T_g, T_d and diffuser outlet T_o (Eq. (4)):

$$\gamma = \frac{T_o - T_g}{T_d - T_o}. \tag{4}$$

The condensation efficiency η is expressed in terms of steam mass flow rate at the gas inlet $\dot{m}_g$ and diffuser outlet $\dot{m}_o$. It describes how much steam has been condensed in the mixing chamber and diffuser (Eq. (5))

$$\eta = \left(1 - \frac{\dot{m}_o}{\dot{m}_g}\right) \cdot 100\%. \tag{5}$$

3.4. Models and governing equations

The mixture model, based on the Euler-Euler approach, is used to calculate multiphase flow. The governing equations of mass, momentum and energy are presented in Eqs. (6)–(8), and volume fractions of water, steam and CO_2 are presented in

Eqs. (9)–(11). The momentum conservation equation (Eq. (7)) uses cylindrical coordinates because the axisymmetric model is used. It is assumed that the circumferential velocity and the circumferential gradients are zero.

$$\int_A \rho_m \boldsymbol{v}_m \cdot d\boldsymbol{a} = 0, \tag{6}$$

$$\oint_{\partial A} \rho_m (\boldsymbol{v}_m \boldsymbol{v}_m) \cdot \boldsymbol{r} ds = -\oint_{\partial A} p\mathbf{I} \cdot \boldsymbol{r} ds + \oint_{\partial A} \mathbf{T}_m \cdot \boldsymbol{r} ds +$$

$$+ \int_A \frac{1}{r} \begin{bmatrix} 0 \\ p - \tau_{\theta\theta} \\ 0 \end{bmatrix} \cdot \boldsymbol{r} dA + \int_A \boldsymbol{f}_b \, dA, \tag{7}$$

$$\int_A \rho_m H_m \boldsymbol{v}_m \cdot d\boldsymbol{a} = -\int_A \dot{\boldsymbol{q}} \cdot d\boldsymbol{a} +$$

$$+ \int_A (\mathbf{T}_m \cdot \boldsymbol{v}_m) \cdot d\boldsymbol{a} + \int_V (\boldsymbol{f}_b \cdot \boldsymbol{v}_m + S_e) \cdot dV, \tag{8}$$

$$\int_A \alpha_w \boldsymbol{v}_m \cdot d\boldsymbol{a} = \int_V S_w \, dV + \int_A \frac{\mu_t}{\mathrm{Sc}_t \rho_m} \nabla \alpha_w \cdot d\boldsymbol{a}, \tag{9}$$

$$\int_A \alpha_s \boldsymbol{v}_m \cdot d\boldsymbol{a} = \int_V S_s \, dV + \int_A \frac{\mu_t}{\mathrm{Sc}_t \rho_m} \nabla \alpha_s \cdot d\boldsymbol{a}, \tag{10}$$

$$\int_A \alpha_{CO2} \boldsymbol{v}_m \cdot d\boldsymbol{a} = \int_A \frac{\mu_t}{\mathrm{Sc}_t \rho_m} \nabla \alpha_{CO2} \cdot d\boldsymbol{a}. \tag{11}$$

In Eq. (7), $\boldsymbol{v}_m = (v_z v_r v_\theta)^T$ and the third right hand side term contains a tensor $\begin{bmatrix} 0 \\ p - \tau_{\theta\theta} \\ 0 \end{bmatrix}$.

The realizable two-layer $k–\varepsilon$ model was used to calculate turbulence. The turbulent dynamic viscosity μ_t is calculated according to Eq. (12). Two transport equations for turbulent kinetic energy are solved: for turbulent kinetic energy k (Eq. (13)) and turbulent dissipation rate ε (Eq. (14)).

$$\mu_t = \rho C_\mu f_\mu kT, \tag{12}$$

$$\nabla \cdot (\rho k \overline{v}) = \nabla \cdot \left[\left(\mu + \frac{\mu_t}{\sigma_k} \right) \nabla k \right] + P_k - \rho(\varepsilon - \varepsilon_o) + S_k, \tag{13}$$

$$\nabla \cdot (\rho \varepsilon \overline{v}) = \nabla \cdot \left[\left(\mu + \frac{\mu_t}{\sigma_\varepsilon} \right) \nabla \varepsilon \right] + \frac{1}{t_e} C_{\varepsilon 1} P_\varepsilon +$$

$$- \rho C_{\varepsilon 2} f_2 \left(\frac{\varepsilon}{t_e} - \frac{\varepsilon_o}{t_0} \right) + S_\varepsilon. \tag{14}$$

The condensation is calculated using a thermally driven model where the rate of boiling/condensation depends on heat transfer between saturated interphase boundary surfaces and phases. The interphase mass flow rate $\dot{g}$ per unit volume between steam s and water w can expressed as in Eq. (15)

$$\dot{g}^{(s\,w)} = \frac{Q_s^{(s\,w)} + Q_w^{(s\,w)}}{L_{s\,w}}. \tag{15}$$

One of the parameters that determine the heat transfer rate Q is the heat transfer coefficient h (Eq. (16)). It depends on the continuous phase (steam) heat conductivity λ_c, Nusselt Number Nu and interaction length scale l (droplet diameter)

$$h^{(s\,w)} = \frac{\lambda_c Nu}{l}. \tag{16}$$

The Nusselt number was calculated using the Ranz-Marshal approach supplemented with the Armenante-Kirwan correlation [32] for condensation on water droplets (Eq. (17))

$$\mathrm{Nu} = 2 + 0.6 \mathrm{Re}_t^{0.5} \mathrm{Pr}_c^{0.33}. \tag{17}$$

The Nusselt Number, thereby the heat transfer coefficient has been corrected by the correlation from Borishanskiy et al. [33], (Eq. (18)), where $\overline{h}_{co_2}$ denotes the heat transfer coefficient with inert gas and $\overline{h}$ – in the absence of inert gas

$$\frac{\overline{h}_{co_2}}{\overline{h}} = 1 - 0.25 \cdot (\alpha_{CO_2})^{0.7}. \tag{18}$$

Validation has been developed based on the results from the spray ejector condenser experimental rig located at AGH for the same boundary conditions. A detailed description of the design of the experimental rig and measurement devices is presented by Madejski et al. [34]. Pressure sensors were located near the wall at gas and water inlets, and temperature sensors were at the ejector outlet. A good agreement is obtained for the gas inlet pressure and outlet temperature, and moderate agreement for the water inlet pressure (see Table 2).

Table 2. Validation of the CFD results.

	Gas inlet pressure, bar	Water inlet pressure, bar	Outlet temperature, K
CFD	0.97	13.5	327.33
Experiment	0.95	15.6	321.60
Error, %	2.3	13.5	1.8

4. Results

4.1. Motive nozzle diameter

The following nozzle diameters are considered: 2.6 mm, 2.8 mm, 3.0 mm (basic mode), 3.2 mm, and 3.6 mm for various types of boundary conditions at the water inlet: velocity and pressure. Figure 5 shows the pressure contours located in the suction chamber for various motive nozzle diameters for a constant velocity boundary condition at the water inlet. The pressure difference is high: from 7 bar for the largest nozzle diameter (3.6 mm) to 23 bar for the smallest one (2.6 mm).

Cross-sectional average pressure and steam mass flow charts along the flow path for velocity and pressure boundary condi-
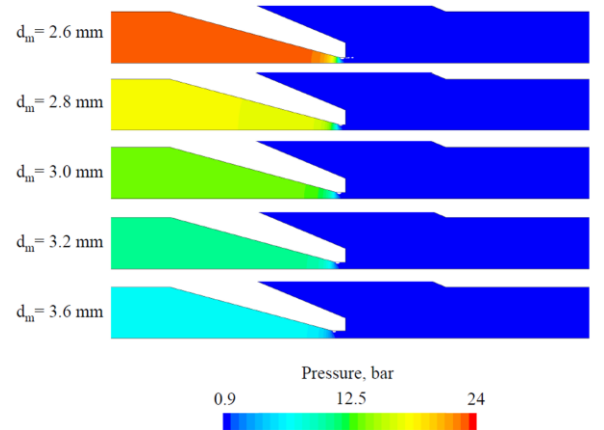

Fig. 5. Pressure contours in the suction chamber for various motive nozzle diameter for constant velocity boundary conditions.

tions (b.c.) at the water inlet are presented in Figs. 6, 7 and Figs. 8, 9, respectively. Considering the constant velocity (mass flow rate) at the water inlet: smaller nozzle diameters create a greater sub-pressure at the gas inlet (up to 0.91 bar) and intensify the condensation process, which can be noticed in the more rapid decrease in steam mass flow. A reverse trend can be noticed for pressure boundary conditions at the water inlet: better
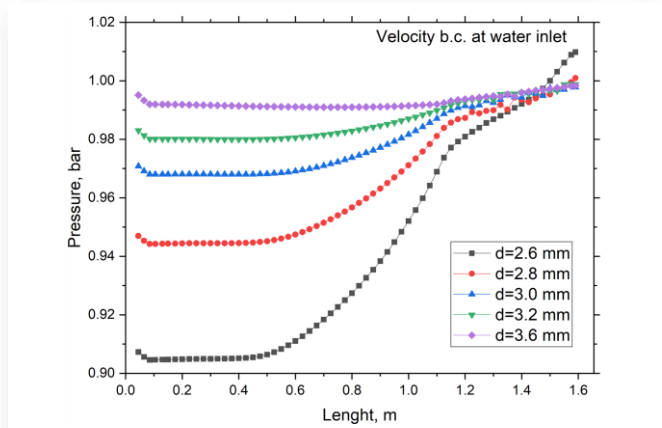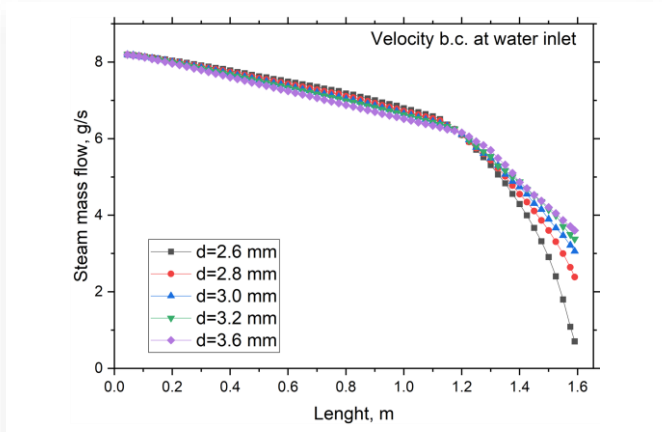

Fig. 8. Average steam mass flow change along the flow path for velocity b.c. at water inlet (0 mm – motive nozzle outlet).
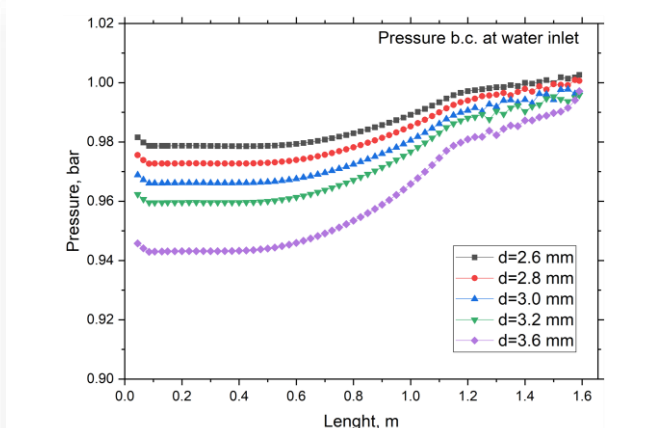
Fig. 6. Average pressure change along the flow path for velocity b.c. at water inlet (0 mm – motive nozzle outlet).
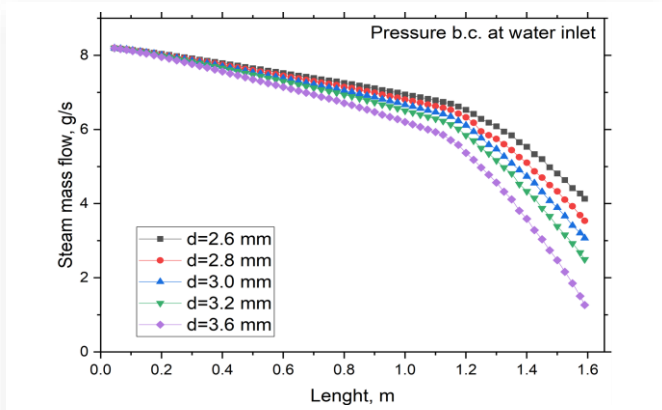

Fig. 9. Average steam mass flow change along the flow path for pressure b.c. at water inlet (0 mm – motive nozzle outlet).

performance (condensation insensitivity, lower gas inlet pressure) is achieved for nozzles with higher diameters.

Velocity contours for various nozzle diameters are presented in Fig. 10 and Fig. 11 for velocity and pressure b.c. at the water inlet, respectively. The highest velocity occurs in the region of the water jet, especially at the beginning of the mixing chamber. Considering constant velocity b.c. at the water inlet (constant mass flow rate), the smaller the nozzle diameter, the higher the velocity of the mixture.

Fig. 7. Average pressure change along the flow path for pressure b.c. at water inlet (0 mm – motive nozzle outlet).
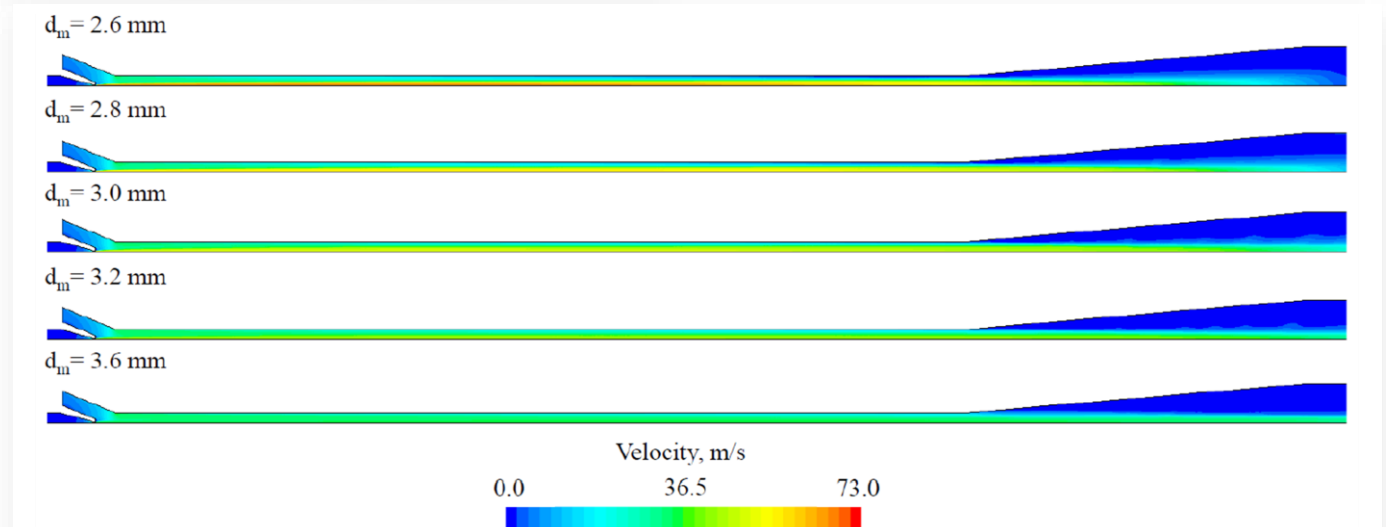

Fig. 10. Velocity contours for various nozzle diameters for constant velocity b.c.
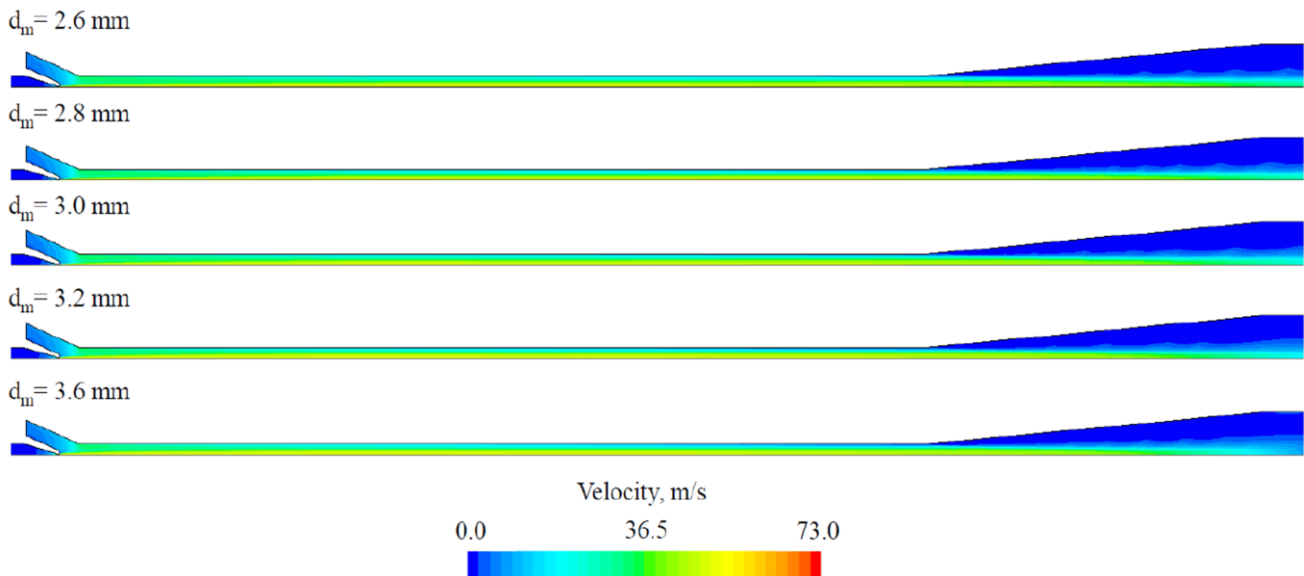
Fig. 11. Velocity contours for various nozzle diameters for constant pressure b.c.

The maximum velocity of about 70 m/s is achieved for the nozzle diameter 2.6 mm, and it occurs near the ejector axis. For the 3.6 mm diameter, the mixture velocity in the mixing chamber is uniform and about 30 m/s. Regarding velocity contours for pressure b.c. differences are not clearly visible between different nozzles diameters. The mixture velocity does not exceed 50 m/s.

Steam volume fraction contours for various nozzle diameters for velocity b.c. are presented in Fig 12. Lower values of steam volume fraction occur in the water jet region. Some part of the steam still exists near the outlet in all cases.

The performance analysis based on non-dimensional ejector indicators for different motive nozzle diameters considering two types of b.c. (velocity and pressure) is presented in Table 3. The compression ratio ranges between 1.003–1.113 and the pressure ratio 0.0017–0.0046. The maximum value is obtained for the motive nozzle diameter 2.6 mm for velocity b.c. Considering pressure b.c., the greatest compression ratio is obtained for the motive nozzle diameter 3.6 mm (1.054 and 4.844, respectively) but it is connected with quite a low mass entrainment ratio (0.0205). Considering the condensation efficiency, it varies significantly depending on the b.c. type at the water inlet and motive nozzle diameter. The highest 91.4% is obtained for the motive nozzle diameter 2.6 mm and velocity b.c. at the water inlet. The lowest 49.6% is achieved for the same motive nozzle diameter but for pressure b.c. at the water inlet.
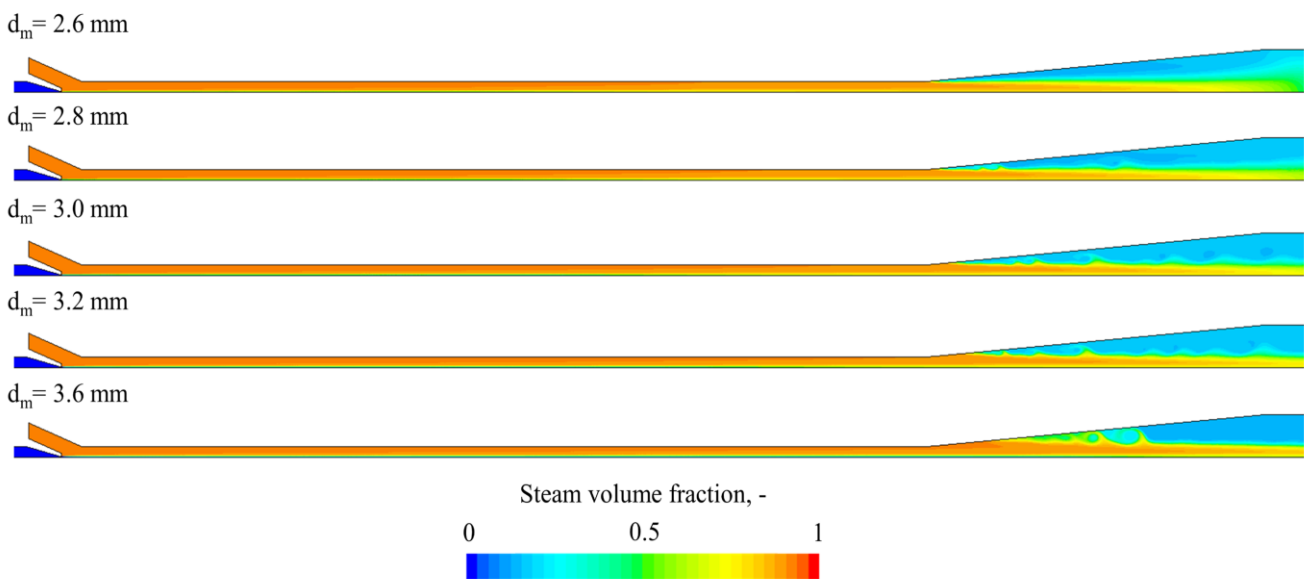

Fig. 12. Steam volume fraction contours for various nozzle diameters for constant pressure b.c.

Kuś T., Madejski P.

Table 3. Performance analysis for various motive nozzle diameters using different b.c. at the water inlet.

B.c. at the water inlet		Motive nozzle diameter, mm	Compression ratio ξ,	Expansion ratio Θ,	Pressure ratio N,	Mass entertainment ratio ω$_M$,	Temperature ratio γ,	Condensation efficiency η, %
Velocity		2.6	1.113	25.506	0.0046	0.0295	2.972	91.4
		2.8	1.056	18.479	0.0032	0.0295	3.192	70.9
		3.0	1.044	13.912	0.0035	0.0295	3.283	62.7
		3.2	1.016	10.875	0.0016	0.0295	3.356	58.8
		3.6	1.003	7.131	0.0005	0.0295	4.526	56.0
Pressure		2.6	1.021	13.759	0.0017	0.0394	2.319	49.6
		2.8	1.025	13.843	0.0020	0.0339	2.769	56.8
		3.0	1.047	13.937	0.0036	0.0295	3.243	62.5
		3.2	1.034	14.031	0.0026	0.0259	3.691	69.5
		3.6	1.054	14.275	0.0041	0.0205	4.844	84.5

4.2. Mixing chamber diameter

Three mixing chamber diameters are taken into account: 20 mm, 25 mm (basic mode), and 30 mm. The mixing chamber diameter can be manipulated in two ways: shortening the size of the exhaust gas inlet line or slightly reducing the length of the mixing chamber (marked as *). The cross-sectional average pressure and temperature charts for the various mixer diameters are presented respectively in Fig. 13 and Fig. 14. Increasing the diameter of the mixing chamber causes the outlet temperature to be higher. It indicates that the condensation process is more intensive. Reducing the diameter leads to a decrease in the performance of the ejector: pressure losses can be observed in the mixing chamber, and outlet temperature is reduced.

Figure 15 shows the velocity contours for different mixing chamber diameters. A significantly higher mixture velocity (45−55 m/s) for a 20 mm mixing chamber diameter is observed. It can be the reason for the high-pressure losses. Moreover, the highest value of velocity occurs in the water jet region for 25 mm and 30 mm mixing chamber diameters. For the 20 mm diameter, the velocity value is high in the gas region near the mixing chamber wall.

Temperature contours for various mixing chamber diameters are presented in Fig 16. The differences in the radial direction are visible. With a 20 mm mixing chamber diameter, the temperature becomes uniform much more quickly. Fluctuation of the temperature in the diffuser can be observed due to the mixing and condensation processes.
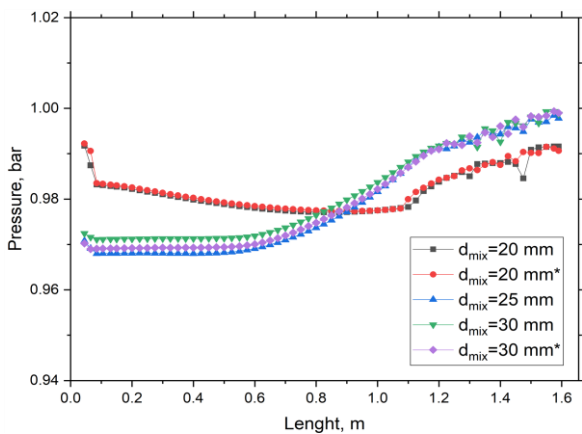

Fig. 13. Average pressure change along the flow path for various mixing chamber diameters (0 mm – motive nozzle outlet).
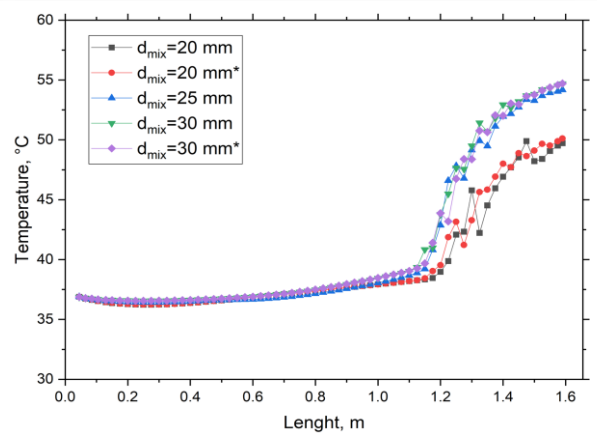

Fig. 14. Average pressure change along the flow path for various mixing chamber diameters (0 mm – motive nozzle outlet).
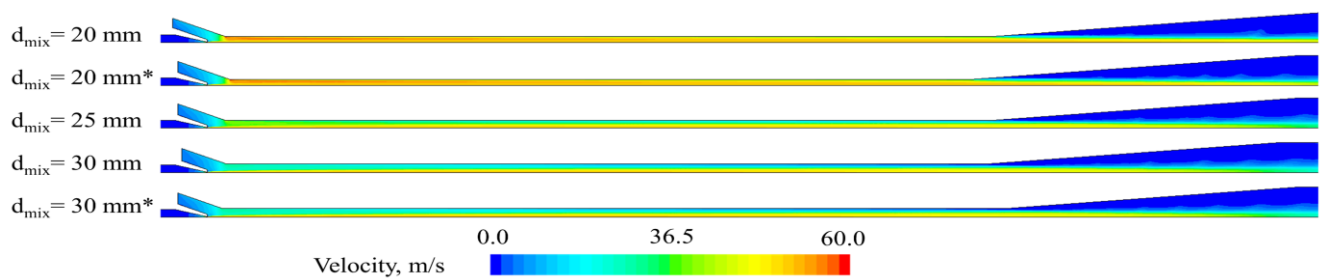

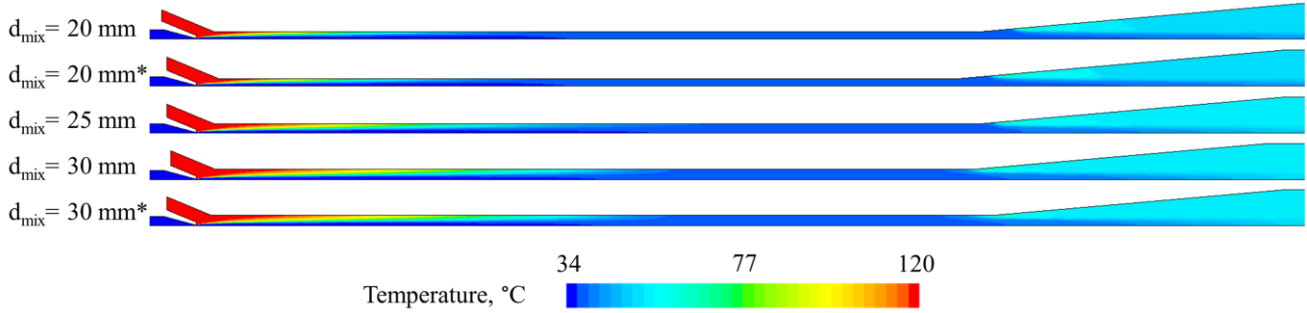Fig. 15. Velocity contours for various mixing chamber diameters.

80

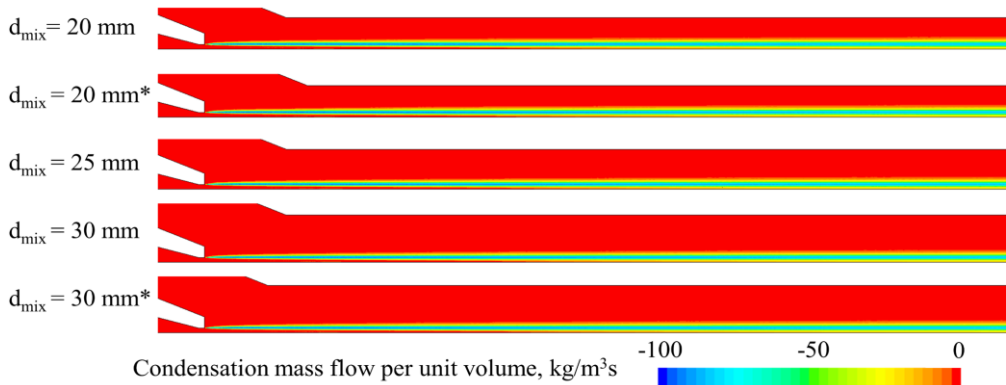Fig. 16. Temperature contours for various mixing chamber diameter.

Fig. 17. Condensation mass flow contours for various mixing chamber diameter.

Table 4. Performance analysis for various mixing chamber diameter.

Mixing chamber diameter, mm	Compression ratio ξ,	Expansion ratio θ,	Pressure ratio N,	Mass entertainment ratio ω_M,	Temperature ratio k,	Condensation efficiency η, %
20	0.999	13.646	-0.0001	0.0295	4.534	57.9
20*	0.998	13.651	-0.0002	0.0295	4.393	59.8
25	1.044	13.912	0.0035	0.0295	3.283	62.7
30	1.027	13.894	0.0021	0.0295	3.178	68.1
30*	1.029	13.928	0.0023	0.0295	3.171	66.8

Condensation mass flow contours for various mixing chamber diameters are presented in Fig. 17. The condensation occurs mainly in the water jet region. The maximum value of condensation mass flow per unit volume is about 100 kg/m³s. There are no clear differences between the contours for different mixing chamber diameters.

Performance analysis using performance ejector indicators for various mixing chamber diameters is presented in Table 4. The highest compression ratio is achieved for the 25 mm mixing chamber diameter (basic mode). Considering the 20 mm mixing chamber diameter, no pressure lift is observed because the compression ratio is around 1. An increase in the mixing chamber diameter causes the compression ratio and temperature ratio to be lower. The mass entrainment ratio is the same for all considering cases because of constant mass flow rate/velocity b.c. at the water and gas inlet. The condensation efficiency is higher for the increased mixing chamber diameter.

5. Conclusions

An axisymmetric CFD model of the ejector condenser was developed to investigate the ejector performance and condensation intensity for various design modes. The presence of three phases – water, steam and CO_2 was considered using the mixture model. A thermally-driven model with the applied Nusselt correlation for direct contact condensation was used to calculate the condensation. A mesh independence test and the comparison with the experimental results were performed. The analysis considered two geometrical parameters: motive nozzle diameter (for two types of b.c. at the water inlet) and mixing chamber diameter.

Changing the diameter of the motive nozzle significantly affects the generated pressures and the efficiency of vapour condensation. For the assumed constant flow rate of the motive wa-

ter, decreasing the diameter from 3.0 mm to 2.6 mm is more profitable: lower pressure at the gas inlet and less steam at the outlet (better condensation intensity). For the assumed constant pressure at the motive water inlet, increasing the diameter from 3.0 mm to 3.6 mm improves the compression effect and condensation performance.

Reducing the mixing chamber diameter from 25 mm to 20 mm diameter causes a significant growth in the velocity of the mixture and leads to pressure losses and a decrease in the condensation efficiency. Increasing the diameter to 30 mm decreases the compression ratio by about 1.5%, and the condensation efficiency by about 6.5%–8.6%.

Results show that the developed CFD model which reflects multiphase turbulent flow with phase change in the spray ejector can be helpful for investigating thermal-flow phenomena and assessing the influence of the chosen geometric parameters on the ejector performance. Results also indicate the direction of further design improvements. Future work should investigate other geometrical parameters that can significantly affect the performance.

Acknowledgements

References

[1] Croquer, S., Poncet, S., & Aidoun, Z. (2016). Turbulence modeling of a single-phase R134a supersonic ejector. Part 1: Numerical benchmark. *International Journal of Refrigeration*, 61, 140-152. doi: 10.1016/j.ijrefrig.2015.07.030

[2] Aidoun, Z., Ameur, K., Falsafioon, M., & Badache, M. (2019). Current Advances in Ejector Modeling, Experimentation and Applications for Refrigeration and Heat Pumps. Part 1: Single-phase ejector. *Inventions*, 4(1). doi: 10.3390/inventions4010015

[3] de Oliveira Marum, V.J., Reis, L.B., Maffei, F.S., Ranjbarzadeh, S., Korkischko, I., dos Santos Gioria, R., & Meneghini, J.R. (2021). Performance analysis of a water ejector using Computational Fluid Dynamics (CFD) simulations and mathematical modeling. *Energy*, 220. doi: 10.1016/j.energy.2021.119779

[4] Xiao, J., Wu, Q., Chen, L., Ke, W., Wu, C., Yang, X., Yu, L., & Jiang, H. (2022). Assessment of Different CFD Modeling and Solving Approaches for a Supersonic Steam Ejector Simulation. *Atmosphere*, 13(1), 144. doi: 0.3390/atmos13010144

[5] Ringstad, K.E., Allouche, Y., Gullo, P., Ervik, A., & Banasiak, K. (2022). A detailed review on CO2 two-phase ejector flow modeling. *Thermal Science and Engineering Progress*, 20. doi: 10.1016/j.tsep.2020.100647

[6] Koirala, R., Inthavong, K., & Date, A. (2022). Numerical study of flow and direct contact condensation of entrained vapor in water jet eductor. *Experimental and Computational Multiphase Flow*, 4, 291–303. doi: 10.1007/s42757-021-0118-2

[7] Zheng, P., Li, B., & Qin, Jingxuan. (2018). CFD simulation of two-phase ejector performance influenced by different operation conditions. *Energy*, 155, 1129–1145. doi 10.1016/j.energy.2018.04.066

[8] Assari, M.R., Tabrizi, H.B., Beik, A.J.G., & Shamesri, K. (2022). Numerical Study of Water-air Ejector using Mixture and Two-phase Models. *International Journal of Engineering*, 35(2), 307−318. doi: 10.5829/IJE.2022.35.02B.06

[9] Sharma, D., Patwardhan, A., & Ranadek, V. (2018). Effect of turbulent dispersion on hydrodynamic characteristics in a liquid jet ejector. *Energy*, 164, 10–20. doi: 10.1016/j.energy.2018.08.171

[10] Wang, X., Li, H., Dong, J., Wu, J. & Tu, J. (2020). Numerical study on mixing flow behavior in gas-liquid ejector. *Experimental and Computational Multiphase Flow*, 3, 108–112. doi: 10.1007/s42757-020-0069-z

[11] Majchrzyk, M., Dziurowicz, D., Hajda, M., Palacz, M., Bodys, J., Fingas, R., Smolka, J., & Nowak, A.J. (2020). Detailed numerical investigation of the CO two-phase ejector 3-D CFD model based on the flow visualisation experiments. *Chemical Engineering and Processing - Process Intensification*, 182. doi: 10.1016/j.cep.2022.109195

[12] Madejski, P., Banasiak, K., Ziółkowski, P., Mikielewicz, D., Mikielewicz, J., Kuś, T., Karch, M., Michalak, P., Amiri, M., Dąbrowski, P., Stasiak, K., Subramanian, N., & Ochrymiuk, T. (2023). Development of a spray-ejector condenser for the use in a negative CO_2 emission gas power plant, *Energy*, 283. doi: 10.1016/j.energy.2023.129163

[13] Reis, L.B., & dos Santos Gioria, R. (2021). Optimization of liquid jet ejector geometry and its impact on flow fields. *Applied Thermal Engineering*, 194. doi: 10.1016/j.applthermaleng.2021.117132

[14] Sheha, A.A.A., Nasr, M., Hosien, M.A., & Wahba, E.M. (2018). Computational and Experimental Study on the Water-Jet Pump Performance. *Journal of Applied Fluid Mechanics*, 11(4), 1013–1020. doi: 10.29252/jafm.11.04.28407

[15] Zhang, J., Geng, J., Yang, S., Cheng, C. Zhu, G., Wang, C., Yang, Z., & Lye, Y. (2023). Influence of geometric parameters on the performance of ejector used in aeroengine air system. *Thermal Science and Engineering Progress*, 37(1). doi: 10.1016/j.tsep.2022.101571

[16] Chen, W., Huang, C., Bai, Y., Chong, D., Yan, J., & Liu, J. (2020). Experimental and numerical investigation of two phase ejector performance with the water injected into the induced flow. *International Journal of Advanced Nuclear Reactor Design and Technology*, 2, 15–24. doi: 10.1016/j.jandt.2020.01.001

[17] Yan, J., Shu, Y., Jiang, J., & Wen, H. (2023). Optimization of Two-Phase Ejector Mixing Chamber Length under Varied Liquid Volume Fraction. *Entropy*, 2023, 25(1). doi: 10.3390/e25010007

[18] Mohammadi, A. (2019). An investigation of geometrical factors of multi-stage steam ejectors for air suction. *Energy*, 186. doi: 10.1016/j.energy.2019.07.138

[19] Foroozesh, F., Khoshnevis, A.B., & Lakzian, E. (2020). Investigation on the effects of water steam ejector geometry in the refrigeration systems using entropy generation assessment. *Journal of Thermal Analysis and Calorimetry*, 141, 1399–1411. doi: 10.1007/s10973-019-09128-1

[20] Dong, J., Hu, Q., Yu, M., Han, Z., Cui, W., Liang, D., Ma, H., & Pan, X. (2020). Numerical investigation on the influence of mixing chamber length on steam ejector performance. *Applied Thermal Engineering*, 174. doi: 10.1016/j.applthermaleng.2020.115204

[21] Han, Y., Wang, X., Sun, H., Zhang, G., Guo, L., & Tu, J. (2019). CFD simulation on the boundary layer separation in the steam

ejector and its influence on the pumping performance. *Energy*, 167. doi: 10.1016/j.energy.2018.10.195

[22] Weber, C. (1931). On the disintegration of a liquid jet. *Zeitschrift für Angewandte Mathematik und Mechanik*, 11(2), 136–154. doi: 10.1002/zamm.19310110207

[23] Mikielewicz, D., Amiri, M., & Mikielewicz, J. (2022). Direct-contact condensation from vapour-gas mixture in a spray ejector condenser for negative CO_2 power plant. *2nd International Conference on Negative CO_2 Emissions*, June 14–17, Gothenburg, Sweden.

[24] He, S., Li, Y., & Wang, R.Z. (2009). Progress of mathematical modelling on ejectors. *Renewable and Sustainable Energy Reviews*, 18(3), 1760–1780. doi: 10.1016/j.rser.2008.09.032

[25] Colarossi, M., Trask, N., Schmidt. D.P., & Bergander, M.J. (2012). Multidimensional modeling of condensing two-phase ejector flow. *International Journal of Refrigeration*, 35(2), 290–299. doi: 10.1016/j.ijrefrig.2011.08.013

[26] Ameur, K., Aidoun, Z., & Ouzzane, M. (2016). Modeling and numerical approach for the design and operation of two-phase ejectors. *Applied Thermal Engineering*, 109, 809–818. doi: 10.1016/j.applthermaleng.2014.11.022

[27] Madejski, P., Michalak, P., Karch, M., Kuś, T., & Banasiak, K. (2022). Monitoring of Thermal and Flow Processes in the Two-Phase Spray-Ejector Condenser for Thermal Power Plant Applications. *Energies*, 15(19). doi: 10.3390/en15197151

[28] Madejski, P., Karch, M., Michala, P., & Banasiak, K. (2024). Conceptual Design of Experimental Test Rig for Research on Thermo-Flow Processes During Direct Contact Condensation in the Two-Phase Spray-Ejector Condenser. *Journal of Energy Resources Technology*, 146(3). doi: 10.1115/1.4064194

[29] Ziółkowski, P., Madejski, P., Amiri, M., Kuś, T., Stasiak, K., Subramanian, N., Pawlak-Kruczek, H., Badur, J., Niedźwiedzki, Ł., & Mikielewicz, D. (2021). Thermodynamic Analysis of Negative CO2 Emission Power Plant Using Aspen Plus, Aspen Hysys, and Ebsilon Software. *Energies*, 14(19), 6304. doi: 10.3390/en14196304

[30] Wagner, W., & Kretzschmar, H.-J. (2008). *International Steam Tables—Properties of Water and Steam Based on the Industrial Formulation IAPWS-IF97. Tables, Algorithms, Diagrams, and CD-ROM Electronic Steam Tables – All of the Equations of IAPWS-IF97 Including a Complete Set of Supplementary Backward Equations for Fast Calculations of Heat Cycles, Boilers, and Steam Turbines*, 2nd Ed. Springer, New York.

[31] Linstrom, P.J., & Mallard, W.G. (2001). The NIST Chemistry WebBook: A Chemical Data Resource on the. *Journal of Chemical and Engineering Data*, 46(5), 1059–1063. doi: 10.1021/je000236i

[32] Armenante, P.M., & Kirwan, D.J. (1989). Mass Transfer to microparticles in agitated Systems. *Chemical Engineering Science*, 44(12), 2781–2796. doi: 10.1016/0009-2509(89)85088-2

[33] Borishanskiy, V.M. (1977). Effect of Uncondensable Gas Content on Heat Transfer in Steam Condensation in a Vertical Tube. *Heat Transfer - Soviet Research*, 9, 35–42.

[34] Madejski, P., Karch, M., Michalak, P., & Banasiak, K. (2024). Conceptual Design of Experimental Test Rig for Research on Thermo-Flow Processes During Direct Contact Condensation in the Two-Phase Spray-Ejector Condenser. *Journal of Energy Resources Technology*, 146(3), 1–39. doi: 10.1115/1.4064194